


RESEARCH ARTICLE

Optical and magneto-optical properties of pulsed laser-deposited thulium iron garnet thin films

Apoorva Sharma¹ | Oana T. Ciubotariu² | Patrick Matthes³ | Shun Okano¹ | Vitaly Zviagin⁴ | Jana Kalbáčová^{1,5} | Sibylle Gemming^{6,7} | Cameliu Himcinschi⁸ | Marius Grundmann⁴ | Dietrich R. T. Zahn^{1,7} | Manfred Albrecht² | Georgeta Salvan^{1,7} 

¹Semiconductor Physics, Institute of Physics, Chemnitz University of Technology, Chemnitz, Germany

²Institute of Physics, University of Augsburg, Augsburg, Germany

³Fraunhofer Institute for Electronic Nanosystems, Chemnitz, Germany

⁴Felix-Bloch-Institut für Festkörperphysik, Universität Leipzig, Leipzig, Germany

⁵HORIBA Jobin Yvon GmbH, Oberursel, Germany

⁶Theoretical Physics of Quantum Mechanical Processes and Systems, Institute of Physics, Chemnitz University of Technology, Chemnitz, Germany

⁷Center of Materials, Architectures and Integration of Nanomembranes, Chemnitz University of Technology, Chemnitz, Germany

⁸Institute of Theoretical Physics, TU Bergakademie Freiberg, Freiberg, Germany

Correspondence

Georgeta Salvan, Semiconductor Physics, Institute of Physics, Chemnitz University of Technology, Reichenhainerstr. 70, 09107 Chemnitz, Germany.
Email: salvan@physik.tu-chemnitz.de

Funding information

Deutsche Forschungsgemeinschaft

Abstract

This work presents a combined optical and magneto-optical spectroscopic study of thulium iron garnet ($\text{Tm}_3\text{Fe}_5\text{O}_{12}$, TmIG) films on substituted gadolinium gallium garnet ($\text{Gd}_{2.6}\text{Ca}_{0.4}\text{Ga}_{4.1}\text{Mg}_{0.25}\text{Zr}_{0.65}\text{O}_{12}$, sGGG) substrates. Spectroscopic ellipsometry, transmission spectroscopy, magneto-optical Kerr effect spectroscopy and Raman spectroscopy results are presented for TmIG films with a thickness in the range from 20 to 300 nm grown on sGGG by pulsed laser deposition. The complex dielectric functions of TmIG and sGGG are determined and compared with previously published results for bulk yttrium iron garnet and GGG, respectively. The magneto-optical spectroscopy corroborated with Raman spectroscopy sheds light on strain-induced changes as a function of TmIG film thickness.

KEYWORDS

magneto-optical Kerr spectroscopy, Raman spectroscopy, spectroscopic ellipsometry, substituted gadolinium gallium garnet, thulium iron garnet

INTRODUCTION

Garnets are complex orthosilicate minerals that have been used for several centuries as semiprecious gemstones. Among the vast family of garnets, magnetic garnets are of special interest due to their

unique properties, such as ferromagnetic insulators [1], ultra-low magnetization damping [2] and high magneto-optical response [3], as well as strong and tunable magnetic anisotropy [4]. Such properties make magnetic garnets indispensable materials for applications including optical isolators [5], insulator spintronics [6, 7], data storage

This is an open access article under the terms of the [Creative Commons Attribution](https://creativecommons.org/licenses/by/4.0/) License, which permits use, distribution and reproduction in any medium, provided the original work is properly cited.

© 2023 The Authors. *Applied Research* published by Wiley-VCH GmbH.

[8, 9] and magneto-optical displays [10]. A quintessential property for high-density storage or other device applications of garnets is the transformation of the magnetic anisotropy from out-of-plane (OOP) to in-plane (IP), depending on the choice of the substrate [11–14], film-thickness [15] and crystallographic orientation [16]. Tang et al. [17] demonstrated that lattice mismatch-induced strain in ferromagnetic garnet epilayers can be harnessed to promote strong OOP anisotropy. Often gadolinium gallium garnet (GGG), a synthetic garnet crystal, is used as a substrate for the growth of ferromagnetic garnet films due to its symmetry-equivalent crystal structure (lattice constant 12.381–12.385 Å) and its typically low defect density [18, 19]. However, its lattice parameters are too small to ensure the epitaxial growth of substituted iron garnets. To overcome this issue, usually, the native GGG crystal structure is altered by the coupled substitution of gallium by magnesium and zirconium, and gadolinium by calcium, resulting in a lattice constant of 12.505 Å [20]. Using such an altered garnet as a substrate, Ciubotariu et al. [15] demonstrated an OOP ($K_U = 9 \pm 2 \text{ kJ/m}^3$) to IP ($K_U = 3 \pm 0.2 \text{ kJ/m}^3$) magnetic anisotropy transition for pulsed laser-deposited (PLD) thulium iron garnet ($\text{Tm}_3\text{Fe}_5\text{O}_{12}$, TmIG) films with increasing film thickness from 20 to 300 nm. They attributed this transformation to the relaxation of the compressive strain, present in the thin films due to the lattice mismatch between the TmIG (111) film and the substituted gadolinium gallium garnet ($\text{Gd}_{2.6}\text{Ca}_{0.4}\text{Ga}_{4.1}\text{Mg}_{0.25}\text{Zr}_{0.65}\text{O}_{12}$, sGGG) (111) substrate. Recently, Moodera's group presented the possibility of further tuning the magnetic anisotropy in an epitaxial TmIG/Au/TmIG multilayer structure for obtaining an even stronger perpendicular magnetic anisotropy, which is useful in spintronic devices [21]. Therefore, it is of utmost importance to investigate and understand the electronic structure of TmIG thin films and the influence of strain on the electronic states.

Here, we report on the room temperature magneto-optical and optical properties of thin film thicknesses in the range from 20 to 300 nm deposited on sGGG substrates using PLD. The optical and magneto-optical properties were assessed by SE and MOKE spectroscopy, respectively. The results reveal a strong dependence of the magneto-optical spectra on the film thickness that we relate to the effect of strain relaxation with increasing film thickness. A thickness-dependent Raman spectroscopy study was performed to probe the strain in the TmIG thin films. Furthermore, we present the first extensive study of bulk sGGG using SE in the spectral range from 0.73 to 5.0 eV.

MATERIALS AND METHODS

Materials

Pristine, defect-free GGG has the composition $\text{Gd}_3\text{Ga}_5\text{O}_{12}$ (GGG) [19]. It crystallizes in the body-centred cubic space group 230, $la\bar{3}d$ ($m\bar{3}m$; O_h^{10}) with a lattice constant of 12.38–12.41 Å at ambient conditions [22, 23]. Crystal field parameters were obtained in good correspondence between experimental and theoretical data for the

following occupation of the Wyckoff positions: Gd at the 24c site, Ga at the 16a and 24d sites and O at the 96h site [24]. Crystallographic and Raman reference data can be obtained from repositories such as the one created by the RRUFF project under data set number X090006 [25]. Pristine GGG was observed to be a frustrated antiferromagnet down to 25 mK [26], which requires (weak) external fields to develop long-range order [27, 28]. Further thermodynamic and spectroscopic data are available from the Materials Project under data set number mp-2921 [29] and references therein.

The substrate material employed here is partly substituted by Ca, Mg and Zr; thus, it exhibits a stoichiometry $\text{Gd}_{3-x}\text{Ca}_x\text{Ga}_{5-x-2y}\text{Mg}_y\text{Zr}_{x+y}\text{O}_{12}$ ($x = 0.4$ and $y = 0.25$) and an expanded lattice constant of 12.50 Å. The ordered parent compounds are the triclinic (P-1), ferromagnetic insulator $\text{CaCd}_2\text{ZrGa}_4\text{O}_{12}$ [30] and the cubic garnet $\text{Gd}_3\text{Ga}_4\text{Mg}_{0.5}\text{Zr}_{0.5}\text{O}_{12}$ with a lattice constant of 12.49 Å [31, 32]. The $\text{CaCd}_2\text{ZrGa}_4\text{O}_{12}$ lattice is close to a symmetric body-centred cubic ($la\bar{3}d$) crystal with a corresponding cubic lattice constant of 12.66 Å with minor deviations of 0.03 Å. Concerning the fully cubic structure, Zr substitutes regularly on the Ga 16a sites and Ca occupies specific ones of the Gd 24c sites. In $\text{Gd}_3\text{Ga}_4\text{Mg}_{0.5}\text{Zr}_{0.5}\text{O}_{12}$ both Mg and Zr reside on the Ga 16a sites; the maximum lattice expansion to 12.49 Å is achieved for $y = 0.54$, the two-phase region starts from $y > 0.7$ onwards.

The terahertz determination of the response functions of pristine and Sc-doped GGG [33] indicates that at least Sc substitution does not significantly change the low-temperature THz Faraday rotation, low-loss and nondispersive optical response properties of the pristine material.

Bulk TmIG is a ferromagnetic insulator, which exhibits a body-centred cubic symmetry with space group $la\bar{3}d$ (space group 230, point group $m\bar{3}m$; O_h^{10}) and a lattice constant of 12.45 Å. Fe occupies the 16a and the 24d Wyckoff positions, Tm resides on the 24c sites and O on the 96h sites forming the typical garnet oxygen sublattice, which is also present in the GGG substrate (see [34] and references therein). Density functional band structure calculations indicate that the 4f electrons of Tm do not significantly influence the crystal structure or the magnitude of the local magnetic moments on the Fe sites [35]. Perpendicular magnetic anisotropy was observed in epitaxially strained (111) oriented TmIG films on a pristine GGG substrate [36].

The oxygen atoms of both parent compounds occupy the same 96h positions of the $la\bar{3}d$ space group, with (x, y, z) coordinate triples of (0.40015, 0.30275, 0.22259) in bulk GGG and of (0.40182, 0.30876, 0.22526) in bulk TmIG. In relative coordinates, the positional mismatch amounts to 0.00676 or about 0.7%. For identical lattice constants, the two sublattices would thus be able to grow epitaxially on top of each other with only a marginal local excess volume relative to the bulk crystals. As the relative coordinate changes in the two oxides close to the boundary amount only to 0.3%–0.4%, we can expect the GGG/TmIG interface energy to be lower than the sum of the two surface energies.

The lattice constant of the GGG substrate is, however, larger than the one of bulk TmIG by 0.0107 or 1.07%. Thus, TmIG is under

moderate tensile strain parallel to the interface plane if it grows epitaxially on GGG (111). This tensile strain can lead to a reduction of the lattice constant in the TmIG film perpendicular to the interface, at least in the interface-near region, and limits the achievable epitaxial film thickness.

Sample preparation

Single-crystal sGGG (111) substrates of composition $Gd_{3-x}Ca_xGa_{5-x-2y}Mg_yZr_{x+y}O_{12}$ ($x=0.4$ and $y=0.25$) with a lattice constant $a = 12.50 \text{ \AA}$ in dimensions size $5 \text{ mm} \times 5 \text{ mm} \times 0.5 \text{ mm}$ were acquired from MaTeck Material-Technologie & Kristalle GmbH. A single-side polished sGGG crystal was used for the SE measurements and similar substrates were used to grow TmIG films. TmIG thin films were deposited using the PLD technique from a commercially available polycrystalline 4 N pure TmIG target, procured from G-Materials GmbH. Before deposition, the target was preconditioned in high vacuum (10^{-6} mbar) with 10,000 laser ($\lambda = 248 \text{ nm}$) pulses of pulse duration 20 ns at an energy of 300 mJ. For a conformal deposition, the samples were placed ~ 4 cm away in the direct line of sight to the target. The temperature of the substrate was monitored with a thermocouple placed on the sample holder and maintained at 615°C . A small quantity of silver paste was used to improve the thermal conductivity between the substrate and the sample holder. The deposition conditions (oxygen pressure of 0.04 mbar, laser energy 300 mJ and pulse frequency of 2 Hz) were kept the same for all samples. After the deposition, the samples were cooled at a rate of $-13^\circ\text{C}/\text{min}$. These deposition conditions were found to yield stoichiometric TmIG films [15]. The deposition rate was calibrated using Rutherford backscattering spectrometry and the structural and magnetic properties of the films were investigated in detail in a previous study by Ciubotariu et al. [15].

Spectroscopic ellipsometry

In ellipsometry, the relative change in polarization of the reflected light from a sample is recorded in terms of the ellipsometric angles ψ and Δ defined in Equation (1)

$$\tan(\psi)e^{i\Delta} = \frac{r_s}{r_p} = \rho, \quad (1)$$

where r_s and r_p are the Fresnel reflection coefficients for s- and p-polarized light. Their ratio ρ is, in the case of an ideal film grown onto a semiinfinite substrate, a function of the complex refractive indices of air (n_0, k_0), of the film (n_1, k_1) and of the substrate (n_2, k_2), of the thickness of the layer (t_1), of the angle of incidence (α) and the wavelength (λ) [37]. In practice, the layer has a certain surface roughness or is covered by contaminants that can influence the optical response as well.

The SE measurements were performed using an M2000 ellipsometer (rotating compensator ellipsometer) from J. A. Woollam

Co. Inc. in the spectral range from 0.73 to 5.0 eV for the sGGG samples and the TmIG films. All measurements were conducted in ambient conditions.

The optical dielectric functions of the samples under study were extracted from the experimental ψ and Δ data by fitting the parametrized optical function model (referred to as the optical model throughout this work) to the experimental data by an iterative, nonlinear regression method implemented in the proprietary software CompleteEASE[®] from J. A. Woollam Co. Inc. The goodness of the fits was quantified by the root-mean-squared error (MSE) value calculated as

$$MSE_{NCS} = \sqrt{\frac{1}{3n-m} \sum_{i=1}^n \left[\left(\frac{N_{Ei} - N_{Gi}}{0.001} \right)^2 + \left(\frac{C_{Ei} - C_{Gi}}{0.001} \right)^2 + \left(\frac{S_{Ei} - S_{Gi}}{0.001} \right)^2 \right]}, \quad (2)$$

where n is the number of spectral data points and m is the number of fit parameters in the optical model. The parameters N , C and S are defined as: $N = \cos(2\psi)$, $C = \sin(2\psi)\cos(\Delta)$ and $S = \sin(2\psi)\sin(\Delta)$. A detailed description of the N , C and S parameters can be found elsewhere [38]. The typical precision in measuring the N , C and S parameters is ≈ 0.001 , hence this factor is included in the MSE definition, implying that an ideal data modelling should have an MSE of ≈ 1 [38].

sGGG substrate

The SE parameters ψ and Δ as a function of wavelength were recorded at seven angles of incidence (AOI) ranging from 45° to 75° over the spectral range of 248–1700 nm (5.0–0.73 eV) in steps of 2.5 nm. The optical constants of sGGG were derived from the experimental data by fitting the optical model using an extended Cauchy dispersion model

$$n(\lambda) = A + \frac{B}{\lambda^2} + \frac{C}{\lambda^4}, \quad (3)$$

$$k(E) = k_0 e^{E-E_g}. \quad (4)$$

Here, A , B and C are fit parameters that govern the line shape of $n(\lambda)$. The absorption tail $k(E)$ is described by the parameters amplitude of absorption (k_0), and band edge (E_g). Additionally, a Bruggemann effective medium approximation (BEMA) 50% void:50% sGGG of thickness 4.0 nm was added in the optical model to account for surface roughness, similar to Jellison and Modine [39].

TmIG films on sGGG substrates

The ψ and Δ spectra for the TmIG thin film samples were measured at AOIs from 45° to 70° in steps of 5° in the spectral range of 246–1700 nm (5.0–0.73 eV). For the data analysis, a layer-by-layer

optical model was designed, where the optical constants derived from the sGGG SE analysis were used to model the bottom layer and the optical dispersion of the top layer accounting for TmIG was addressed using a GENOSC-layer (see Equation 5), which comprises two Lorentzian (see Equation 6) and a Tauc-Lorentzian oscillator (see Equation 7), mathematically implemented as

$$\varepsilon_{\text{TmIG}}(E) = 1 + \varepsilon_{\text{T-L}}(E) + \varepsilon_{\text{Lorentz-1}} + \varepsilon_{\text{Lorentz-2}} \quad (5)$$

A Lorentz dispersion formula for the n th oscillator is given as (Equation 6)

$$\varepsilon_L(E) = \frac{A_n \Gamma_n E_n}{E_n^2 - E^2 - iE\Gamma_n}, \quad (6)$$

where A_n , Γ_n and E_n are amplitude (unitless), broadening (eV) and central energy (eV) of the n th oscillator, respectively [40]. This oscillator represents the absorption probability of photons with the central energy of E_n in the considered spectral range. Here, the fit parameters are A_n , Γ_n and E_n .

The Tauc-Lorentz dispersion function is a complex function that takes into account the presence of a Lorentzian oscillator as well as the onset of absorption near the bandgap of a material

$$\varepsilon_{\text{T-L}}(E) = \varepsilon_{n1} + i\varepsilon_{n2}, \quad (7)$$

where

$$\varepsilon_{n2}(E) = \frac{A_n E_{0n} \Gamma_n (E - E_g)^2}{(E^2 - E_{0n}^2)^2 + \Gamma_n^2 E^2} \frac{1}{E} \quad \text{for } E > E_g, \quad (8)$$

$$\varepsilon_{n2}(E) = 0 \quad \text{for } E < E_g, \quad (9)$$

and

$$\varepsilon_{n1}(E) = \frac{2}{\pi} P \int_{E_{gn}}^{\infty} \frac{x \varepsilon_{n2}(x)}{x^2 - E^2} dx, \quad (10)$$

where E_{0n} is the central energy of the electronic transition, E_g is the material bandgap and Γ_n is the broadening in eV [39]. As Equation (9) shows, the Tauc-Lorentz dispersion function has the constraint that ε_{n2} is zero below the bandgap, corresponding to the transparent region in the spectra. The fit parameters for the Tauc-Lorentz function in our modelling are A , Γ , E_0 and E_g .

Surface roughness was taken into account with a BEMA layer as a mixture of the dielectric function of TmIG and 50% of voids, with the thickness of the surface roughness layer (t_{rough}) as a fit parameter [41]. Similarly, an intermix layer was considered between TmIG and sGGG substrate and its optical properties are modelled as a 50%:50% mixture of TmIG and sGGG.

For greater confidence in the optical model, the SE data of the 200 and 300 nm thin films were analysed together using a multi-sample analysis approach. In the multisample analysis, the optical constants of the TmIG layer are fitted as common fit parameters for both samples, while the thickness and roughness are independent fit parameters for each sample. For 20-, 50- and 70-nm-thick films,

individual optical data modelling was conducted. The dielectric function of the TmIG obtained for the thicker samples (200 nm and 300 nm) was used as starting parameters and adjusted along with the thickness to fit the ψ and Δ spectra of each thin film sample.

MOKE spectroscopy and magnetometry

A home-built MOKE spectrometer in polar geometry (PMOKE) was utilized to measure the photon energy-dependent Kerr rotation (θ_K) and ellipticity (η_K) [42]. Both $\theta_K(E)$ and $\eta_K(E)$ were recorded within the spectral range of 248–827 nm (5.0–1.5 eV) under an incidence angle of 1.3° and an applied magnetic field of ~1 T. The spot size on the sample was about 0.7 cm². In the PMOKE geometry, the direction of the applied magnetic field is perpendicular to the sample plane. Hysteresis loops were recorded using the same PMOKE spectrometer by sweeping the magnetic field between ± 1 T while recording the changes in θ_K at a fixed photon energy of 2.7 eV. The choice of the photon energy for hysteresis loops is based on the maximum spectral slope in the visible spectral region thus giving the highest sensitivity.

Raman spectroscopy

A LabRam HR 800 spectrometer from Horiba Scientific was employed to perform the Raman spectroscopic measurements in the back-scattering configuration. The spectra were acquired with a $\times 100$ microscope objective using the 514.7 nm line of a Cobolt laser with a laser power of 5 mW. The measurements were performed using a 2400 grooves per millimeter grating and an electron-multiplying charge-coupled detector. The spectral resolution achieved was 1.3 cm⁻¹ (as measured from the linewidth of a neon spectral line).

Each sample was measured in multiple locations (>10) for 120 s with two repetitions. The influence of the laser power was probed to ensure that no heating effect or sample damage takes place with the chosen laser power. The stability of the instrument was monitored during and in between the measurements using the spectrum of a neon lamp to make sure that no instrument-related spectral shifts occurred.

RESULTS AND DISCUSSION

sGGG substrate

The measured ψ and Δ spectra of an sGGG substrate are shown by symbols in Figure 1. Since the SE measurements were conducted on a single-side polished sGGG crystal, the backside reflection is assumed to be negligibly small. To model these data, the optical model shown in the sketch in Figure 2a was employed. This model consists of an extended Cauchy layer to account for the substrate, a BEMA layer accounting for the surface roughness or adsorbents such as water or organic contaminants, and the optical properties of the ambient. The

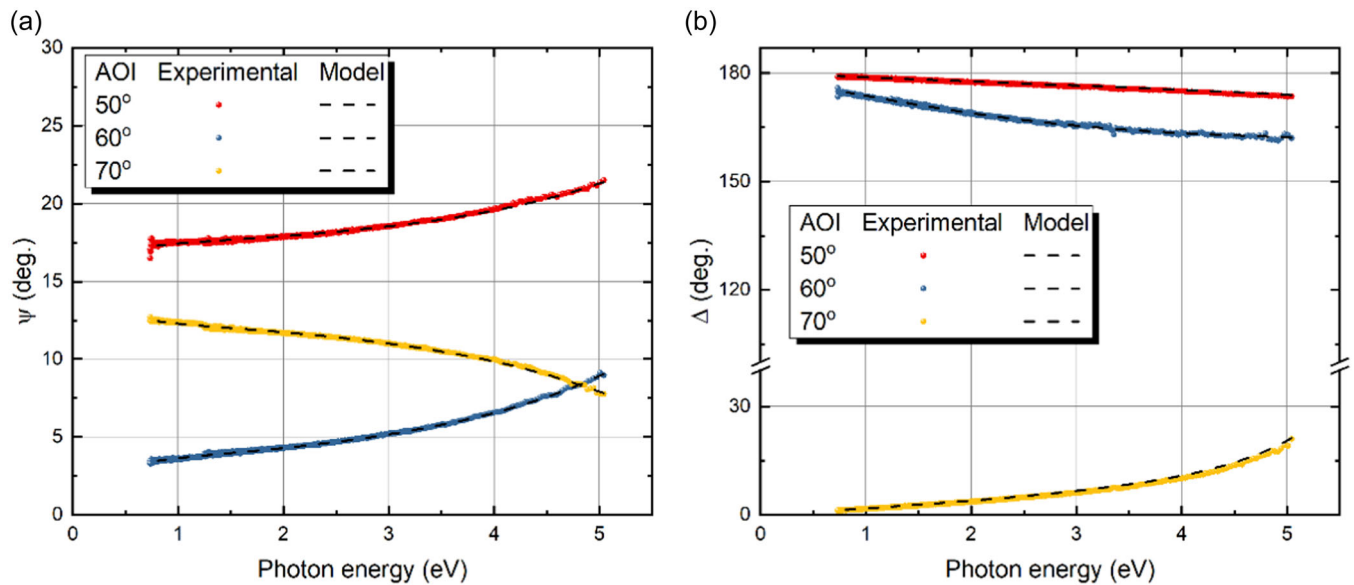


FIGURE 1 Measured spectroscopic ellipsometry data (coloured solid spheres) of the single crystal substituted gadolinium gallium garnet substrate and the corresponding fits using the optical model discussed in the text (dashed line) for $\psi(E)$ (a) and $\Delta(E)$ (b) for the angles of incidence of 50°, 60° and 70°. AOI, angles of incidence.

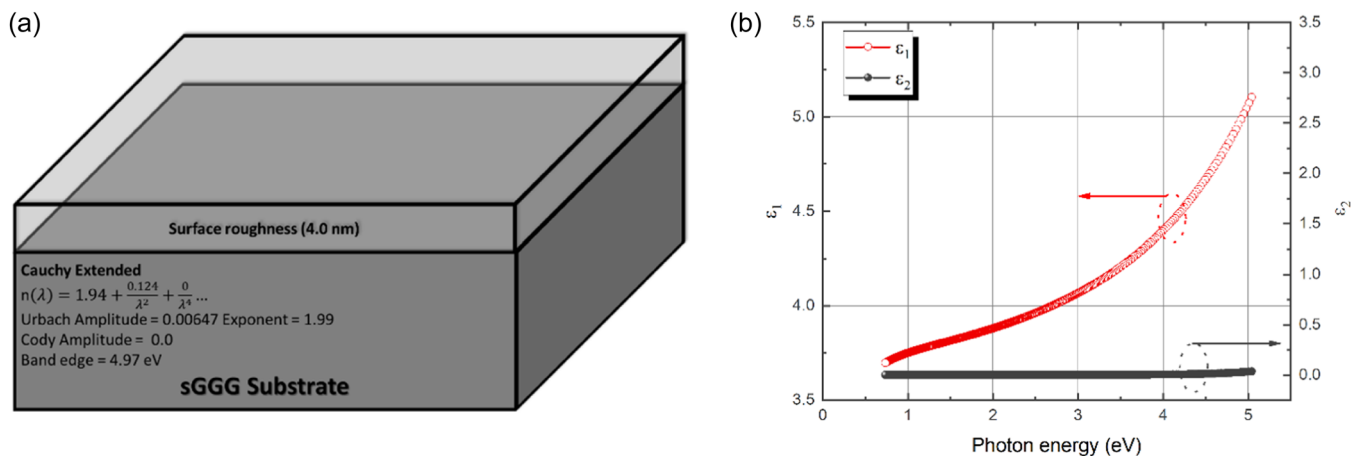


FIGURE 2 (a) Schematic representation of the optical model used to describe the substituted gadolinium gallium garnet (sGGG) substrate. (b) Spectral dependence of the complex dielectric function of the single crystal sGGG, obtained from parametrized optical modelling of the spectroscopic ellipsometry spectra. The real part ϵ_1 and imaginary part ϵ_2 are depicted in red and black, respectively.

substrate was considered as a semi-infinite layer. The band edge value was set to the value of the bandgap estimated from transmission measurements of a double-side polished sample (Supporting Information: Figure S1).

Figure 1 also shows the fit obtained (dashed lines) with the proposed optical model (see Figure 2) for the spectral range of 0.73–5.0 eV. It can be observed that for all considered AOIs, the fit matches very well the experimental data and an MSE value of <1 was achieved after recursive fitting. The dielectric functions obtained from the fit are shown in Figure 2b. These were then considered as fixed parameters in the analysis of the TmIG films on sGGG substrates.

TmIG thin films

The ψ and Δ spectra of the TmIG thin films on sGGG substrates are shown along with the fit data generated from the optical model for 20, 50, 70, 200 and 300 nm thickness in Figure 3. TmIG thickness-dependent strong interference oscillations can be observed in the ψ spectra between 0.73 and 3.5 eV. The period of these oscillations decreases with increasing TmIG film thickness. The Δ spectra, which contain the phase information, are even more sensitive to the thickness variation and show changes below 3.0 eV. The spectra fitted with the optical model are in very good agreement with the experimental spectra, as demonstrated by the low MSE value of ≤ 6

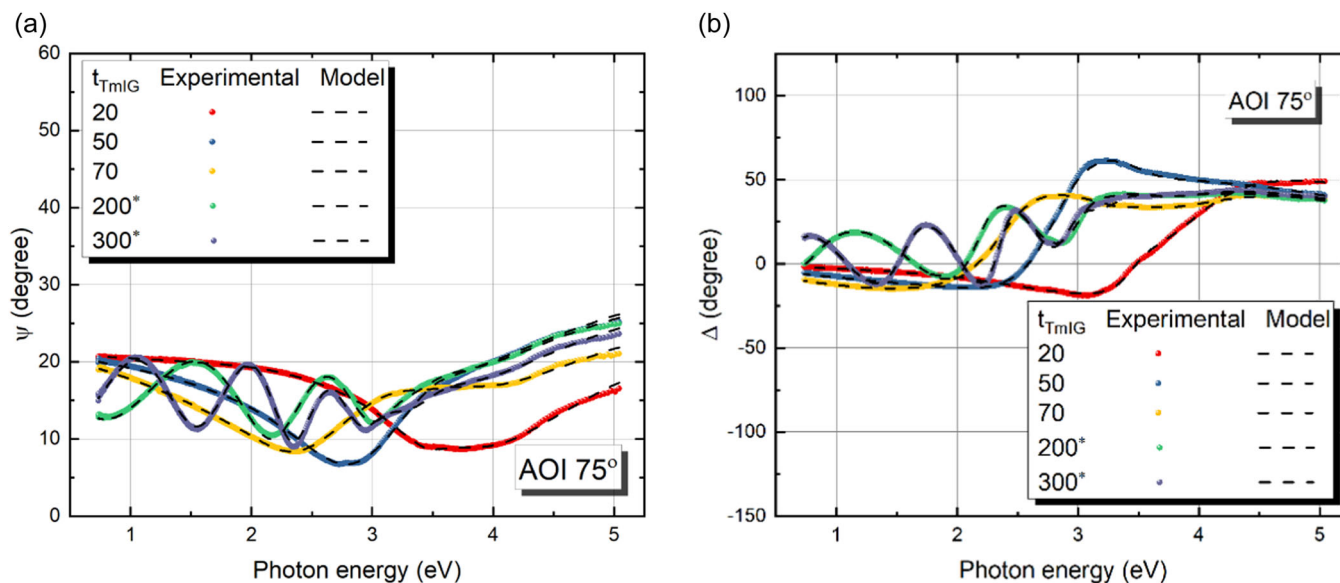


FIGURE 3 The ψ (a) and Δ (b) spectra recorded at angles of incidence (AOI) of 75° for 20-, 50-, 70-, 200- and 300-nm-thick thulium iron garnet (TmIG) film samples are shown in red-, blue-, yellow-, green- and purple-filled circles, respectively. The spectra, generated from the three-layer optical model, are shown with dashed black lines for each sample. The samples marked with * (i.e., 200 and 300 nm) were modelled using a multisample analysis approach.

TABLE 1 Nominal thickness of the TmIG layers along with the thickness and roughness determined from SE data analysis for the studied samples.

Nominal thickness (nm)	Intermix (nm)	Thickness (nm)	Roughness (nm)	MSE
20	4.12 ± 1.0	13.3 ± 0.2	2.5 ± 0.2	4.7
50	2.9 ± 1.0	38.4 ± 0.1	7.4 ± 0.1	3.9
70	3.5 ± 0.2	60.3 ± 0.1	3.2 ± 0.1	3.1
200	3.4 ± 0.5	194.2 ± 0.3	10.1 ± 0.4	5.2* (multisample)
300	3.0 ± 0.5	291.2 ± 0.1	6.5 ± 0.4	5.2* (multisample)

Note: The samples denoted with * were subject of multisample analysis (see Figures 3 and 4 and the corresponding text).

Abbreviations: MSE, (root) mean-squared error; SE, spectroscopic ellipsometry; TmIG, thulium iron garnet.

(see Table 1). The SE-determined thicknesses and the surface roughness of the investigated samples are shown in Table 1. The root-mean-square roughness of the films determined by atomic force microscopy was below 1 nm [15] and, as expected, lower than the roughness value determined from ellipsometry. The two methods probe the roughness at different length scales. Please note that the roughness values determined from the ellipsometry correspond to the best possible fit to the SE data.

The same optical model developed using multisample analysis (200 and 300 nm) was used to model the experimental data of the 20-, 50- and 70-nm-thick TmIG films. However, when simulating the experimental spectra of the thinner films, the main difference was that the amplitude of the Tauc–Lorentz and Lorentz oscillators needed to be adjusted in addition to the thickness to obtain the best fit.

The imaginary part of the dielectric function of TmIG determined by the SE data analysis is shown in Figure 4 along with the oscillators

used for the optical modelling of 200- and 300-nm-thick TmIG film samples. The real and imaginary parts of the complex dielectric function of all studied TmIG films are shown in Figure 4b. The lineshape and the amplitude of the dielectric function of the TmIG are in close agreement with the yttrium iron garnet (YIG) dielectric function reported in the literature [43]. The oscillators positioned at ~ 3.5 and ~ 4.5 eV are analogous to the symmetry-allowed charge transfer transitions of the type $O(2p) \rightarrow Fe(3d)$, as proposed for YIG [43, 44]. Based on the reports on the optical properties of YIG, a strong optical transition corresponding to an $O(2p) \rightarrow Fe(4s)$ inter-band transition is expected above 6.5 eV, and thus the second Lorentzian oscillator was also added to the optical model for taking into account the transitions beyond the measured spectral range. It should be noticed that the spectral line profile and position of spectral features in the dielectric function (cf. Figure 4b) of the 20-, 50- and 70-nm-thick samples are similar to those obtained using the

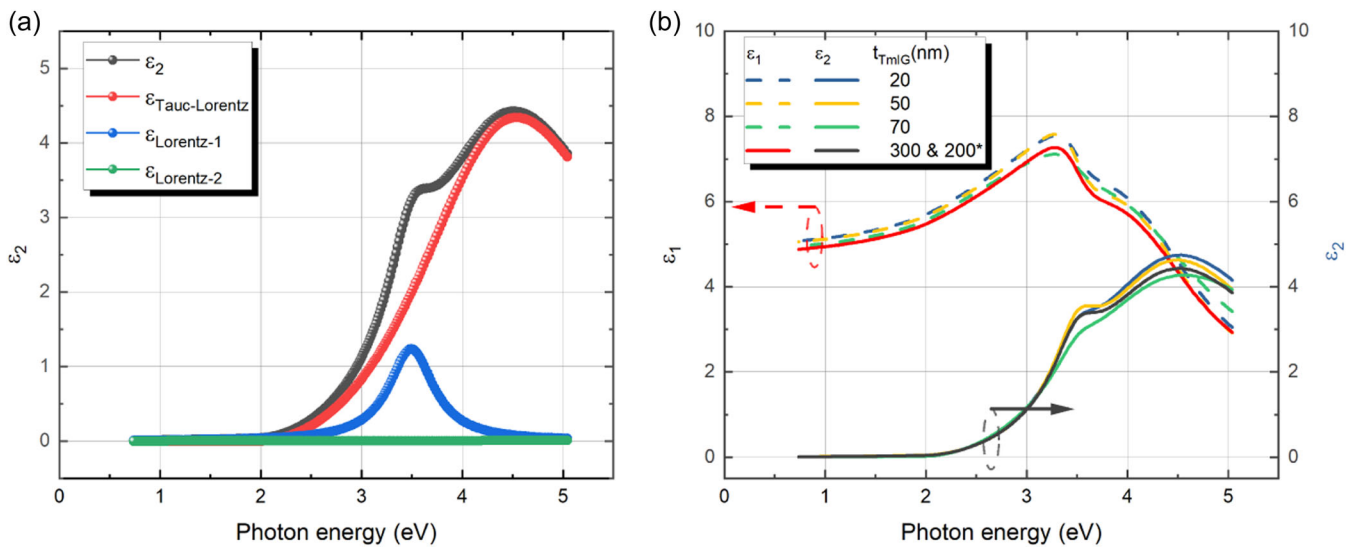


FIGURE 4 (a) The imaginary part of the dielectric function of the thulium iron garnet (TmIG) thin films is shown in black along with the Tauc-Lorentz (red) and the two Lorentzian (green and blue) oscillators used in the optical model for the multisample analysis of the 200- and 300-nm-thick films. (b) The real and imaginary parts of the complex dielectric function (ϵ_1 and ϵ_2) spectra were determined for the TmIG thickness series.

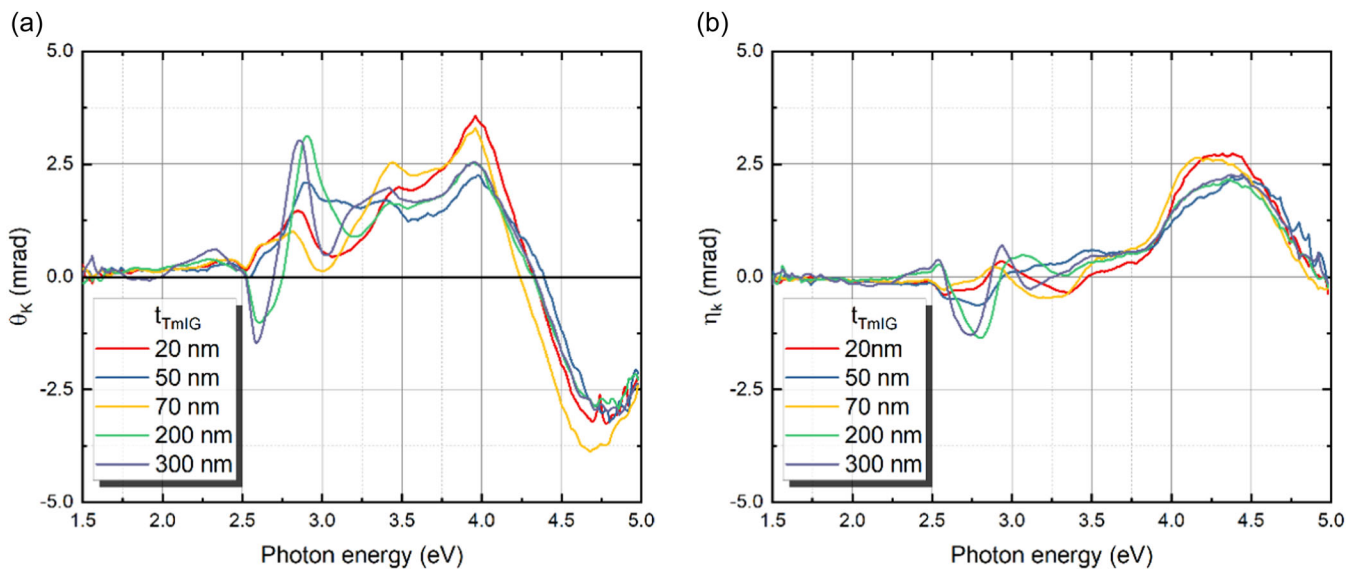


FIGURE 5 (a) Magneto-optical Kerr rotation (θ_K) and (b) Kerr ellipticity (η_K) as a function of photon energy, recorded for different thicknesses of thulium iron garnet (t_{TmIG}).

multisample analysis of the 200- and 300-nm-thick films. The apparent difference in the amplitude of ϵ_1 and ϵ_2 spectra above the bandgap for these samples compared to the other samples can be attributed to the strain. Nevertheless, the changes in spectra are too small to be taken into account as optical anisotropy.

The MOKE spectra recorded for the studied thicknesses of the TmIG thin films are shown in Figure 5. Like YIG, TmIG MOKE spectra are rich in spectral features. Two strong spectral features located at 2.5 and 4.0 eV in TmIG are very similar to those reported by Jakubisova-Liskova and colleagues [45, 46]. A clear distinction can be made between the θ_K spectra of the TmIG film thickness below and

above 70 nm. At lower photon energy, up to ~ 2.5 eV, the θ_K spectra of 20–70-nm-thick films show low amplitudes with subtle spectral details, while the spectral features are more pronounced for the 200- and 300-nm-thick films. Interestingly, no noticeable spectral features can be observed up to 2.5 eV in η_K spectra for the investigated films, independently of the film thickness. In the spectral range between 2.5 and 3.25 eV, very sharp spectral features can be observed for the 200- and 300-nm-thick film, while these spectral features fade as the thickness decreases.

All peaks in the θ_K spectra, ranging from 3.25 to 4.25 eV, exhibit consistent spectral positioning, accompanied by an increase in

spectral amplitude as the TmIG film thickness decreases, except for the 50 nm thickness. This phenomenon could be attributed to two opposing factors: the increase in volume proportional to film thickness and the competition between IP and OOP anisotropy. The latter factor is expected to decrease the MOKE signal in the polar MOKE configuration.

Figure 6 shows the hysteresis loops recorded by PMOKE for the investigated TmIG thin films. It is evident that the 50- and 70-nm-thick films have an OOP magnetic anisotropy as indicated by the square-like loops, with 70 nm showing a larger spread of the switching field distribution, resulting in lower M_r/M_s values (see Figure 6b). The loops recorded for the 200- and 300-nm-thick films show lower coercive fields and M_r/M_s ratios suggesting an IP anisotropy. The increase in the coercive field and M_r/M_s with decreasing TmIG film thickness (see Figure 6b) is associated with the strain in the thin films due to the lattice mismatch, which in turn generates magnetoelastic anisotropy, resulting in an OOP easy axis of magnetization for TmIG thin films. Therefore, we can conclude that with decreasing the film thickness, the stress-induced magnetoelastic anisotropy (that orients the easy magnetization axis out of the sample plane) competes and eventually overcomes the shape anisotropy (that orients the easy magnetization axis in the sample plane), in agreement with previous studies performed by X-ray diffraction [15]. According to Ciubotariu et al. [15], the growth of the TmIG thin film aligns with the (4-44) lattice plane of sGGG up to 50 nm, leading to the presence of only the (4-44) reflex of TmIG in the θ - 2θ scans. However, as the film thickness increases, the (4-44) reflex of TmIG shifts gradually toward the (444) reflex, signifying the relaxation of the TmIG film lattice.

Raman spectroscopy is a known method to evaluate and identify garnet oxides [47, 48]. In addition, it is well known that by tracking shifts in the Raman spectrum, it is possible to determine the strain in

crystal structures [49]. In Figure 7, Raman spectra recorded for different thicknesses of TmIG are shown. The comparison with the reference measurement of sGGG reveals TmIG Raman bands at $\approx 130 \text{ cm}^{-1}$ (T_{2g} optical phonon) and at $\approx 250 \text{ cm}^{-1}$ (E_{2g} optical phonon) that are marked by asterisks. Both bands increase in intensity with increasing TmIG film thickness, although the intensity does not scale linearly.

For the 20-nm-thick TmIG films, there is an obvious shift of the T_{2g} mode toward lower frequencies by 1.5 cm^{-1} compared to the 70 nm TmIG. This can be directly attributed to the strain in the crystal lattice. The 20- and 70-nm TmIG films are very homogeneous, and there is no difference in the sample orientation. Orientation-dependent measurements show a larger value spread for 200- and 300-nm-thick TmIG films, which is connected with larger heterogeneity.

Theoretical calculations

As discussed above, the lattice mismatch of the two bulk materials amounts to about 1%. When grown epitaxially on the sGGG (111) plane, TmIG experiences an IP tensile strain at the interface; thus, a compressive strain may be expected in the direction perpendicular to the TmIG film surface.

To quantify those epitaxy-induced strains and stresses in the TmIG film we performed spin-polarized density functional band structure calculations in the GGA+U approximation by Perdew, Burke and Ernzerhof (PBE) with PAW potentials [50]. We included the 4f electrons of Tm explicitly in the valence band and employed the same numerical settings for that choice as Nakamoto et al. [35] for calculating the ground state properties of the rare-earth iron garnet series.

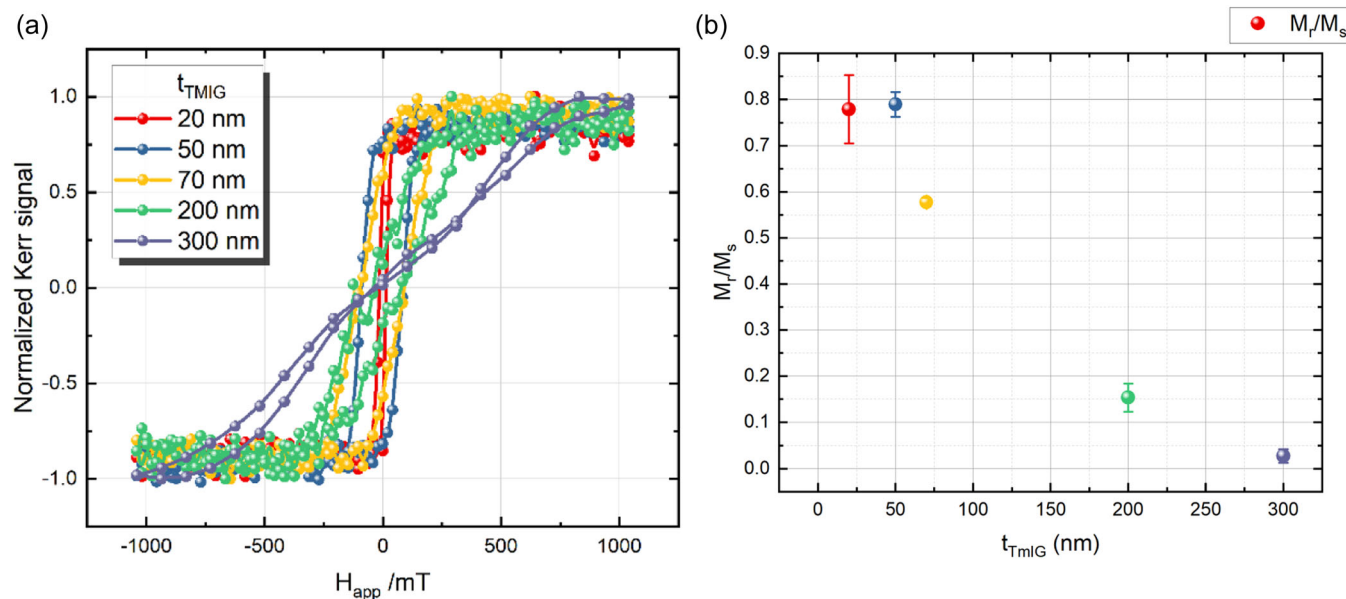


FIGURE 6 (a) Normalized Kerr signal hysteresis loops measured with the magnetic field applied perpendicular to the sample surface for various thicknesses of the thulium iron garnet (TmIG) films. (b) Remanence ratio M_r/M_s versus thickness of TmIG. t_{TmIG} , thicknesses of TmIG.

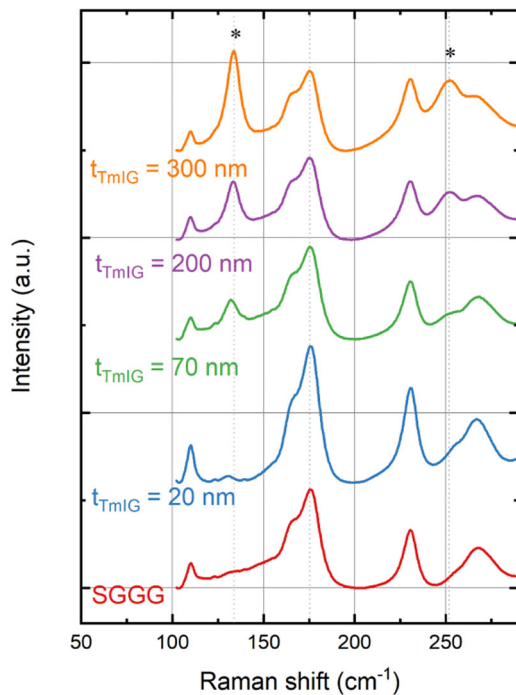


FIGURE 7 Raman spectra of the investigated TmIG film samples and the substituted gadolinium gallium garnet (sGGG) substrate were recorded in the parallel polarization configuration with the light polarization direction parallel to a sample edge. t_{TmIG} , thicknesses of thulium iron garnet.

The relaxed bulk lattice constant of the body-centred TmIG amounts to 10.912 Å, which corresponds to the cubic lattice constant of 12.217 Å reported in Nakamoto et al. [35] for DFT calculations that include the 4f states explicitly. As pointed out there, the calculated lattice constant is slightly lower than the experimental one; this is largely due to the inclusion of Hubbard- U terms with values of 4 eV for the interaction of the Fe 3d and Tm 4f electrons, which are required to represent the electronic structure around the Fermi level appropriately.

The calculated (x, y, z) reduced coordinate triple of O on the 96h sites amounted to (0.4015, 0.3100, 0.2251) for the pristine TmIG, which compares well with the experimental values of (0.40182, 0.30876, 0.22526). This means that the deviation of calculated and experimental oxygen positions is one order of magnitude lower than the strain-relevant difference in oxygen positions in the sGGG and TmIG crystal structures. We can, thus, assume that our DFT calculations allow for an estimate of the strain energy in the TmIG film grown on sGGG.

For mimicking the epitaxial strain of the TmIG layer in the (111) plane, the primitive body-centred unit cell of TmIG was compressively distorted along the [111] direction and the lattice symmetry was reduced to the threefold symmetric rhombohedral space group $R\bar{3}c$ (167). This deformation increases the opening angle between the primitive lattice vectors, and expands also the IP interatomic distances, but shrinks the distances between the (111) lattice planes perpendicular to the interface plane. To find the optimum TmIG structure, which

matches the sGGG lattice epitaxially, the opening angle α was increased from 109.47° to 112° in steps of 0.5°, and the lattice constant was optimized for each opening angle. The energy optimum under the epitaxy constraint is obtained for $\alpha = 110^\circ$ and an expanded lattice constant of 12.226 Å IP. The corresponding density of states curves obtained by gradient-corrected (PBE) density-functional band structure calculations with the projector-augmented plane wave potentials is shown in Supporting Information: Figure S2.

Per formula unit, those distortions build up a strain energy of 0.178 eV. This value corresponds to an upper bound for the strain energy of 0.71 (J/m²)/nm film thickness if the film was strained homogeneously over the whole thickness. As the TmIG lattice is only clamped by the substrate and free to relax towards the film surface, this value reduces to an average value of 0.35 J/m² strain energy/nm film thickness.

To estimate the stable thickness range of the TmIG film this strain energy is assumed to compete with the energy of formation of the free sGGG and TmIG surfaces, which are formed if the film spalls off the substrate upon stress. Depending on the environmental conditions, the typical surface energies of ternary oxides are in the range of 1–3.5 J/m² for stoichiometric, nonpolar surfaces [51, 52]; the work of separation of cubic ternary oxides amounts to up to 5 J/m² on the (100) cleavage planes [53] and may be higher on the polar (111) facets. Thus, cleaving the GGG/TmIG interface into two free surfaces may involve energies of the order of 5 J/m².

From these values, a lower bound for the achievable thickness of a partially strained epitaxial TmIG is estimated as $t_{\text{TmIG}} = 5 \text{ J/m}^2 / 0.35 \text{ (J/m}^2\text{)/nm} \approx 14.3 \text{ nm}$. The TmIG film with the lowest observed thickness of $13.3 \pm 0.2 \text{ nm}$ (nominally 20 nm) and also the lowest roughness is within this range. In contrast, films with measured thickness values of 38.4 and 60.3 nm exhibit a considerably higher surface roughness; even thicker films require a multisample evaluation of the SE measurements. Both types of deviation from the properties of the flat, uniform thinnest film may thus stem from strain release.

CONCLUSION

This study provides a comprehensive understanding of the optical and magneto-optical properties of TmIG thin films on sGGG substrates, with a detailed analysis of the thickness-dependent behaviour of these properties. The results suggest the potential application of TmIG thin films in magneto-optical devices and provide insight into the strain-induced properties of these films. The optical and magneto-optical properties of TmIG thin films with various film thicknesses ($t_{\text{TmIG}} = 50, 70, 200$ and 300 nm) prepared by the PLD technique on sGGG (111) substrate. The complex dielectric function ($\epsilon = \epsilon_1 + i\epsilon_2$) of bulk GGG substituted with Mg, Ca and Zr and the dielectric function of the TmIG were determined using SE. The dielectric function of the TmIG showed a remarkable similarity to YIG.

The magneto-optical Kerr spectra of the measured sample in the photon energy range from 1.5 to 5.0 eV clearly demonstrated the

influence of strain in the thin films, due to the lattice mismatch of the TmIG with the sGGG substrate. The MOKE spectra show the increase in the amplitude of the spectral features with increasing thickness of the TmIG thin film. The magneto-optical transitions between 2.5 and 3.5 eV are marker spectral features for the stress in the thin films that show a blue shift with increasing film thickness. The hysteresis loops recorded using PMOKE showed an OOP magnetic anisotropy for 50- and 70-nm-thick films, while the 200- and 300-nm-thick films showed an IP anisotropy. The increase in the coercive field and M_r/M_s with decreasing TmIG film thickness was associated with the stress-induced magnetoelastic anisotropy competing and eventually overcoming the shape anisotropy.

Raman spectroscopy was used to evaluate and identify garnet oxides, and shifts in the Raman spectrum were used to follow the strain in crystal structures. Spin-polarized density functional band structure calculations were performed to quantify epitaxy-induced strains and stresses in the TmIG film, and the strain energy was found to be an upper bound of $0.71 \text{ (J/m}^2\text{)}/\text{nm}$ film thickness and the lowest thickness predicted for a partially strained epitaxial TmIG was in good agreement with the experiment.

ACKNOWLEDGEMENTS

This work was supported by the Deutsche Forschungsgemeinschaft (DFG) under the project 'Interfacial perpendicular magnetic anisotropy for next-generation monolithic 3D TMR sensors' (Project Number 282193534) and under the project '3D-Strukturierung von dünnen Oxid-Mehrfachschichten mit dem Ionenstrahl' (Project Number 405595647). Open Access funding enabled and organized by Projekt DEAL.

CONFLICT OF INTEREST STATEMENT

The authors declare no conflict of interest.

DATA AVAILABILITY STATEMENT

Data are available from the authors upon reasonable request.

ORCID

Georgeta Salvan  <http://orcid.org/0000-0002-2565-9675>

REFERENCES

- [1] N. Thiery, V. V. Naletov, L. Vila, A. Marty, A. Brenac, J. F. Jacquot, de G. Loubens, M. Viret, A. Anane, V. Cros, J. Ben Youssef, N. Beaulieu, V. E. Demidov, B. Divinskiy, S. O. Demokritov, O. Klein, *Phys. Rev. B* **2018**, *97*, 064422.
- [2] C. N. Wu, C. C. Tseng, Y. T. Fanchiang, C. K. Cheng, K. Y. Lin, S. L. Yeh, S. R. Yang, C. T. Wu, T. Liu, M. Wu, M. Hong, J. Kwo, *Sci. Rep.* **2018**, *8*, 11087.
- [3] M. Gomi, K. Satoh, M. Abe, *Jpn. J. Appl. Phys.* **1988**, *27*, L1536.
- [4] S. Mokarian Zanjani, M. C. Onbaşlı, *J. Magn. Magn. Mater.* **2020**, *499*, 166108.
- [5] T. Mizumoto, R. Takei, Y. Shoji, *IEEE J. Quantum Electron.* **2012**, *48*, 252.
- [6] H. Yu, J. Xiao, P. Pirro, *J. Magn. Magn. Mater.* **2018**, *450*, 1.
- [7] A. Chanda, C. Holzmann, N. Schulz, J. Seyd, M. Albrecht, M. H. Phan, H. Srikanth, *Adv. Funct. Mater.* **2022**, *32*, 2109170.
- [8] K. Shono, S. Kuroda, M. Alex, S. Ogawa, *J. Magn. Magn. Mater.* **1990**, *88*, 205.
- [9] P. Coeure, *J. Phys. Colloq.* **1985**, *46*, C6.
- [10] A. M. Grishin, S. I. Khartsev, S. Bonetti, *Appl. Phys. Lett.* **2006**, *88*, 242504.
- [11] J. Chen, C. Wang, C. Liu, S. Tu, L. Bi, H. Yu, *Appl. Phys. Lett.* **2019**, *114*, 212401.
- [12] J. Fu, M. Hua, X. Wen, M. Xue, S. Ding, M. Wang, P. Yu, S. Liu, J. Han, C. Wang, H. Du, Y. Yang, J. Yang, *Appl. Phys. Lett.* **2017**, *110*, 202403.
- [13] X. Liu, Q. Yang, D. Zhang, Y. Wu, H. Zhang, *AIP Adv.* **2019**, *9*, 115001.
- [14] C. Holzmann, A. Ullrich, O.-T. Ciubotariu, M. Albrecht, *ACS Appl. Nano Mater.* **2022**, *5*, 1023.
- [15] O. Ciubotariu, A. Semisalova, K. Lenz, M. Albrecht, *Sci. Rep.* **2019**, *9*, 17474.
- [16] M. A. Gilleo, *Materials* **1980**, *2*, 1.
- [17] C. Tang, P. Sellappan, Y. Liu, Y. Xu, J. E. Garay, J. Shi, *Phys. Rev. B* **2016**, *94*, 140403.
- [18] J. R. Carruthers, M. Kokta, R. L. Barns, M. Grasso, *J. Cryst. Grow.* **1973**, *19*, 204.
- [19] C. D. Brandle, D. C. Miller, J. W. Nielsen, *J. Cryst. Grow.* **1972**, *12*, 195.
- [20] D. Mateika, R. Laurienand C. Rusche, *J. Cryst. Grow.* **1982**, *56*, 677.
- [21] G. Vilela, H. Chi, G. Stephen, C. Settens, P. Zhou, Y. Ou, D. Suri, D. Heiman, J. S. Moodera, *J. Appl. Phys.* **2020**, *127*, 115302.
- [22] A. Durygin, V. Drozd, W. Paszkowicz, E. Werner-Malento, R. Buczko, A. Kaminska, S. Saxena, A. Suchocki, *Appl. Phys. Lett.* **2009**, *95*, 141902.
- [23] R. Krsmanović, V. A. Morozov, O. I. Lebedev, S. Polizzi, A. Speghini, M. Bettinelli, G. V. Tendeloo, *Nanotechnology* **2007**, *18*, 325604.
- [24] A. Kaminska, R. Buczko, W. Paszkowicz, H. Przybylińska, E. Werner-Malento, A. Suchocki, M. Brik, A. Durygin, V. Drozd, S. Saxena, *Phys. Rev. B: Condens. Matter Mater. Phys.* **2011**, *84*, 075483.
- [25] B. Lafuente, R. T. Downs, H. Yang, N. Stone, unpublished.
- [26] A. P. Ramirez, R. N. Kleiman, *J. Appl. Phys.* **1991**, *69*, 5252.
- [27] O. A. Petrenko, D. McK. Paul, *Phys. Rev. B* **2000**, *63*, 024409.
- [28] N. d'Ambrumenil, O. A. Petrenko, H. Mutka, P. P. Deen, *Phys. Rev. Lett.* **2015**, *114*, 227203.
- [29] Materials Project for $\text{Gd}_3\text{Ga}_5\text{O}_{12}$ (Mp-2921) from database version V2021.11.10.
- [30] Materials Project for $\text{CaGd}_2\text{Zr}(\text{GaO}_3)_4$ (Mp-686296) from database version V2021.11.10, unpublished.
- [31] A. Timm, W. Zimmermann, D. Kollwe, *Nucl. Instr. Methods Phys. Res.* **1982**, *194*, 175.
- [32] D. Mateika, C. Rusche, *J. Cryst. Grow.* **1977**, *42*, 440.
- [33] M. Sabbaghi, G. W. Hanson, M. Weinert, F. Shi, C. Cen, *J. Appl. Phys.* **2020**, *127*, 025104.
- [34] Materials Project for $\text{Tm}_3\text{Fe}_5\text{O}_{12}$ (Mp-1208209) from database version V2021.11.10.
- [35] R. Nakamoto, B. Xu, C. Xu, H. Xu, L. Bellaiche, *Phys. Rev. B* **2017**, *95*, 024434.
- [36] M. Kubota, K. Shibuya, Y. Tokunaga, F. Kagawa, A. Tsukazaki, Y. Tokura, M. Kawasaki, *J. Magn. Magn. Mater.* **2013**, *339*, 63.
- [37] H. Fujiwara, *Spectroscopic Ellipsometry: Principles and Applications*, Wiley, **2007**.
- [38] J. A. Woollam, *CompleteEase Software Manual, Version 4.63*, J. A. Woollam Inc., **2011**.
- [39] G. E. Jellison, F. A. Modine, *Appl. Phys. Lett.* **1996**, *69*, 371.
- [40] F. Wooten, *Optical Properties Of Solids*, 260, Academic Press, **1972**.
- [41] D. A. G. Bruggeman, *Ann. Phys.* **1937**, *421*, 160.
- [42] T. Herrmann, K. Lüdge, W. Richter, K. G. Georgarakis, P. Pouloupoulos, R. Nünthel, J. Lindner, M. Wahl, N. Esser, *Phys. Rev. B* **2006**, *73*, 134408.

- [43] S. H. Wemple, S. L. Blank, J. A. Seman, W. A. Biolsi, *Phys. Rev. B* **1974**, *9*, 2134.
- [44] P. K. Larsen, R. Metselaar, *J. Solid State Chem.* **1975**, *12*, 253.
- [45] E. Jakubisova-Liskova, S. Visnovsky, H. Chang, M. Wu, *J. Appl. Phys.* **2015**, *117*, 17B702.
- [46] P. Hansen, J.-P. Krumme, *Thin Solid Films* **1984**, *114*, 69.
- [47] J.-J. Song, P. B. Klein, R. L. Wadsack, M. Selders, S. Mroczkowski, R. K. Chang, *J. Opt. Soc. Am.* **1973**, *63*, 1135.
- [48] P. Grunberg, J. A. Koningstein, L. G. van Uitert, *J. Opt. Soc. Am.* **1971**, *61*, 1613.
- [49] R. J. Angel, M. Murri, B. Mihailova, M. Alvaro, Z. *Kristallogr Cryst. Mater.* **2019**, *234*, 129.
- [50] X. Gonze, B. Amadon, G. Antonius, F. Arnardi, L. Baguet, J. M. Beuken, J. Bieder, F. Bottin, J. Bouchet, E. Bousquet, N. Brouwer, F. Bruneval, G. Brunin, T. Cavignac, J. B. Charraud, W. Chen, M. Côté, S. Cottenier, J. Denier, G. Geneste, P. Ghosez, M. Giantomassi, Y. Gillet, O. Gingras, D. R. Hamann, G. Hautier, X. He, N. Helbig, N. Holzwarth, Y. Jia, F. Jollet, W. Lafargue-Dit-Hauret, K. Lejaeghere, M. Marques, A. Martin, C. Martins, H. Miranda, F. Naccarato, K. Persson, G. Petretto, V. Planes, Y. Pouillon, S. Prokhorenko, F. Ricci, G. M. Rignanese, A. H. Romero, M. M. Schmitt, M. Torrent, M. J. van Setten, B. Van Troeye, M. J. Verstraete, G. Zérah, J. W. Zwanziger, *Comput. Phys. Commun.* **2020**, *248*, 107042.
- [51] M. Zschornak, S. Gemming, E. Gutmann, T. Weißbach, H. Stöcker, T. Leisegang, T. Riedl, M. Tränkner, T. Gemming, D. C. Meyer, *Acta Mater.* **2010**, *58*, 4650.
- [52] M. Nakayama, K. Ishida, K. Watanabe, N. Tanibata, H. Takeda, H. Maeda, T. Kasuga, *ACS Omega* **2020**, *5*, 4083.
- [53] S. Gemming, G. Seifert, *Acta Mater.* **2006**, *54*, 4299.

SUPPORTING INFORMATION

Additional supporting information can be found online in the Supporting Information section at the end of this article.

How to cite this article: A. Sharma, O. T. Ciubotariu, P. Matthes, S. Okano, V. Zviagin, J. Kalbáčová, S. Gemming, C. Himcinschi, M. Grundmann, D. R. T. Zahn, M. Albrecht, G. Salvan, *Appl. Res.* **2024**;3:e202200064.
<https://doi.org/10.1002/appl.202200064>